PHYSICAL REVIEW E **90**, 042501 (2014)

Theoretical predictions of disclination loop growth for nematic liquid crystals under capillary confinement

Alireza Shams,[1] Xuxia Yao,[2] Jung Ok Park,[2,3] Mohan Srinivasarao,[2,3,4] and Alejandro D. Rey[1,*]
[1]*Department of Chemical Engineering, McGill University, Montreal, Quebec H3A 0C5, Canada*
[2]*School of Materials Science and Engineering, Georgia Institute of Technology, Atlanta, Georgia 30332, USA*
[3]*Center for Advanced Research on Optical Microscopy, Georgia Institute of Technology, Atlanta, Georgia 30332, USA*
[4]*School of Chemistry and Biochemistry, Georgia Institute of Technology, Atlanta, Georgia 30332, USA*
(Received 22 April 2014; published 14 October 2014)

The combination of low elasticity modulus, anisotropy, and responsiveness to external fields drives the rich variety of experimentally observed pattern formation in nematic liquid crystals under capillary confinement. External fields of interest in technology and fundamental physics are flow fields, electromagnetic fields, and surface fields due to confinement. In this paper we present theoretical and simulation studies of the pattern formation of nematic liquid crystal disclination loops under capillary confinement including branching processes from a $m = +1$ disclination line to two $m = +1/2$ disclination curves that describe the postnucleation and growth regime of the textural transformation from radial to planar polar textures. The early postnucleation and growth of emerging disclination loops in cylindrical capillaries are characterized using analytical and computational methods based on the nematic elastica that takes into account line tension and line bending stiffness. Using subdiffusive growth and constant loop anisotropy, we found that the solution to the nematic elastica is a cusped elliptical geometry characterized by exponential curvature variations. The scaling laws that govern the loop growth reflect the tension to bending elasticity balance and reveal that the loop dilation rate depends on the curvature and normal velocity of the disclination. The line energy growth is accommodated by the decrease in branch-point curvature. These findings contribute to the evolving understanding of textural transformations in nematic liquid crystals under confinement using the nematic elastic methodology.

DOI: 10.1103/PhysRevE.90.042501 PACS number(s): 61.30.Jf

I. INTRODUCTION

Nematic liquid crystals (NLCs) are anisotropic viscoelastic materials that exhibit the anisotropy of crystals and the fluidity of viscous liquids; their macroscopic orientation is characterized by the unit director vector **n**. Phase transitions, external electromagnetic fields, shear flows, and confinement usually generate singular and nonsingular orientational defects [1–13]. Disclination formation in nematic liquid crystals under confinement is the subject of continuing interest since frustration emanating from fixed orientation at curved bounding surfaces is common in applications [13–18]. Defects in nematic liquid crystals include disclination lines, walls, and point defects [1,19]. A disclination line is characterized by a quantized charge m which specifies the amount of rotation when encircling the line, and the sign (±) associated with the charge denotes the sense of rotation [2]. Since the energy per unit length or line tension associated with a line defect scales with m^2, $\pm 1/2$ lines are energetically preferred [2,9]. As the defect ring has been investigated previously by De Luca and Rey [20], here we focus on the bending effect on the dynamics and kinematics of the radial disclination loops growth. Straight disclinations only store line tension energy since the planes of director gradients are parallel. On the other hand the energy of a planar curved disclination line contains both tension and bending contributions since the planes of director gradients are splayed [7]. In the most general cases of spiral disclinations, additional torsion elasticity arises. This paper considers curved planar disclination loops under capillary confinement. Figure 1 shows a schematic of a $+1/2$ disclination loop attached to $+1$ line segments, relevant to this paper. The splay of the cross-sectional planes as one moves along the line generate line bending stiffness since $\partial \nabla_{\perp} \mathbf{n} / \partial s \neq 0$, where $\nabla_{\perp} \mathbf{n}$ are normal gradients and "s" is the arc length.

Texturing of NLCs under cylindrical capillary confinement with homeotropic anchoring is summarized in a generic texture phase diagram [20,21] shown in Fig. 2, which contains four textures: (i) polar radial (PR) line defect, (ii) planar polar (PP) line defect, (iii) escape radial ring defect (ERRD), and (iv) escape radial (ER) textures. This figure shows the stability range of each texture and provides a wealth of important information on interfacial science, phase transitions, elasticity, and defect physics. For example, the PR-PP boundary describes the defect instability:$m = +1 \rightarrow 2(m = +1/2)$, emanating from the branch point (BP) to form a loop, driven by bulk elasticity reduction, and hence its location on the texture diagram provides information on bulk elasticity.

The nature of the PR → PP transition in principle can be spinodal (SD) or nucleation and growth (NG), but elastic energy estimates show that NG will prevail. In the SD mode the entire $+1$ line splits into two $+1/2$ lines along the entire capillary of length L that separates under charge repulsion. On the other hand in the NG mode, a number "n" of $+1/2$ loops nucleates and grows along the initial $+1$ line. Since the elastic length scale associated with the director **n** is the capillary radius R_c, the distance between the nucleating loops is on the order of $R_c = L/n$. If the energy cost (creating two cores and two interfaces) of splitting a $+1$ line of length L is L_{E} in the SD mode, then the energy of nucleating n loops in the NG

---

[*] Corresponding author: alejandro.rey@mcgill.ca

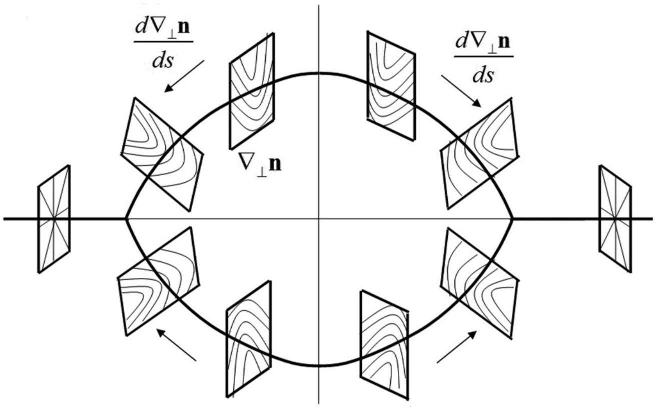

FIG. 1. Schematic of a $+1/2$ disclination loop attached to a $+1$ line and director field in the cross-sectional plane. Disclination bending stiffness arises when $\partial \nabla_\perp \mathbf{n}/\partial s \neq 0$ (adapted from Ref. [7]).

mode is $L_E(R_{\text{loop}}/R_c) < L_E$. Figure 3 shows a schematic of the NG mode of the PR → PP transition consisting of:

(i) *Initial stage*. Nucleation on a preexisting $+1$ line of n $+1/2$ loops separated by a distance on the order of $R_c = L/n$ [Fig. 3(a)].

(ii) *Early stage*. Vertical and horizontal growth of $+1/2$ loops, involving the motion of BPs that join the $+1/2$ loops and the $+1$ line segments with a constant branch angle [see Figs. 3(b) and 4].

(iii) *Intermediate stage*. Coarsening and horizontal growth saturation of the $+1/2$ loops where the vertical saturation is $2y_\infty = 1.33R_c$ [Fig. 3(c)].

(iv) *Late stage*. Formation of the PP texture with two parallel $+1/2$ lines separated by a distance $2y_\infty = 1.33R_c$ [Fig. 3(d)].

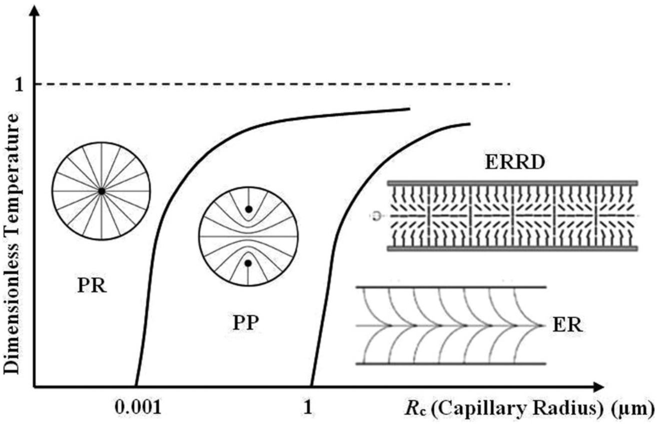

FIG. 2. Texture phase diagram in terms of dimensionless temperature (T/T_{NI}) as a function of the capillary radius for uniaxial nematics under capillary confinement, indicating the geometric and thermal conditions. The horizontal dashed line is the nematic or isotropic transition temperature T_{NI}. PR is the planar radial line defect texture with a $m = +1$ defect at the center, PP is the planar polar line defect texture with two $m = +1/2$ defects, ER is the escaped radial texture where the director tilts out of the cross-sectional plane, and ERRD is the escaped radial ring defect texture, consisting of a periodic lattice of alternating $+1$ and -1 point defects separated by a distance close to the capillary radius (adapted from Ref. [21]).

We emphasize that this paper deals with a single loop growth and that issues with multiple loops, loop-loop interactions, and the exact loop-loop nucleation distance are not considered.

In this paper we only consider the early stage (ii). Stages (iii) and (iv) were discussed in Refs. [7–9,22] where it is shown that the bending to the tension ratio is a function of the capillary geometry. *The key issue of interest in the present paper is as follows: What is the evolving shape of the $+1/2$ disclination loop that reflects the impact of line tension and bending stiffness of disclination lines under given growth kinetics*? In the present problem each of the $+1/2$ disclination loops is attached to a $+1$ string, and they grow driven by the texture transformation process. The related phenomenon of growth of isolated disclination loops in a cylindrical capillary was previously discussed by De Luca and Rey [20].

The organization of this paper is as follows. Section II presents the theoretical framework and equations for disclination loop shape and kinematics. Section III presents the results including disclination curvature and space curve as a function of arc length, the effect of time on the disclination shape and energy, the relations between loop geometry and disclination elasticity, and the kinematics of the disclination loop. Section IV presents the conclusions. The details of the computational method are provided in Appendix A. Appendix B discusses the branch angle shown in Fig. 4 and establishes the relation between the material length scale l_M and the geometric length scale that is behind a fixed branch angle value of 60°, and Appendix C compares the viscous and tension elasticity terms presented in the shape equation. As noted above this paper builds on our previous work on nematic liquid crystals under capillary confinement [7–9].

II. DISCLINATION LOOP SHAPE MODEL AND SIMULATION

A. Disclination loop geometry

Figure 4 shows the (x,y) coordinate system and geometry of a $+1/2$ disclination loop consisting of two planar $m = +1/2$ disclination lines emanating from two branch points located at $(x,y) = [\pm x_b(t),0]$. The semiaxes $[R_x(t),R_y(t)]$ grow in time as dictated by the driving energy minimization.

The unit tangent **t** and the unit normal **N** to the filament are given by [7–9]

$$\mathbf{t}(s,t) = \frac{\partial \mathbf{r}(s,t)}{\partial s}, \tag{1a}$$

$$\frac{\partial t(s,t)}{\partial s} \equiv \frac{\partial^2 \mathbf{r}(s,t)}{\partial s^2} = \boldsymbol{\kappa}\mathbf{N}(s,t), \tag{1b}$$

where $\boldsymbol{\kappa} = \partial \mathbf{t}/\partial s$ is the curvature, $\mathbf{r}$ is the position vector, and s is the arc length, respectively. $\mathbf{t}$ is a unit vector which is expressed with the tangent angle $\varphi(s)$:$\mathbf{t}(s) = [\cos\varphi(s), -\sin\varphi(s)]$. In the normal angle parametrization, the curvature is as follows:$\boldsymbol{\kappa} = \partial\varphi/\partial s \equiv \varphi_s$. According to Fig. 4, to describe the disclination as an evolving space curve $y(x,t)$, we need to specify: (i) the loop curvature $\boldsymbol{\kappa}(s)$, (ii) the tangent angle at the branch point φ_o, (iii) the loop amplitude $R_y(t)$, and (iv) the location of the branch point $R_x(t)$.

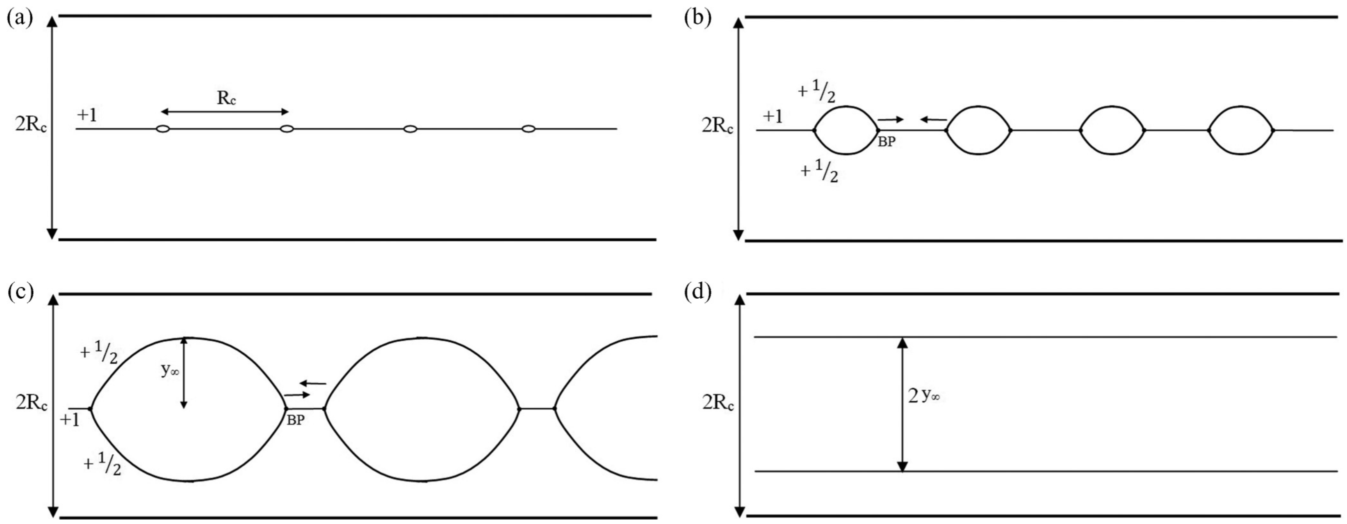

FIG. 3. The nucleation and growth process of domains consisting of +1/2 loops that eventually lead to sections with well-formed PP textures; (a) initial nucleation stage, defect points appear on the +1 disclination line. The distance between two points is on the order of the capillary radius (R_c); (b) early growth stage including textural transitions from high order +1 disclination into energetically less costly +1/2 disclinations. The energy difference between the two textures, which generates the constant motion of the BP; (c) intermediate coarsening stage. The loop expansion stops when the loop vertical radius reaches the final defect distance y_∞ but BPs still move horizontally; (d) final stage. After collision of branch points, we see the relaxation of the line shape leading to 2 +1/2 disclination lines separated by distance y_∞.

B. Disclination shape equation

In this section we derive the disclination shape equation by formulating the force balance equation on the line due to internal and external stresses. Internal stresses include line tension and line bending forces whose expressions are derived using Frank elasticity. The shape equation of the +1/2 disclination is then used to formulate the shape equation for the growing +1/2 loop.

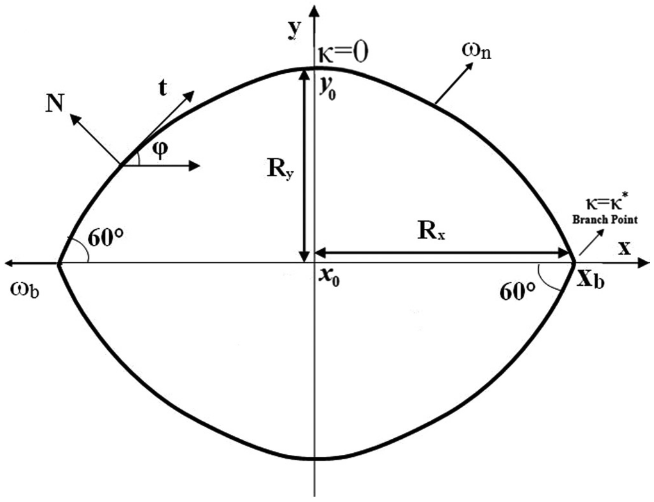

FIG. 4. Schematic of the coordinate system and geometry of two $m = +1/2$ lines emanating from the branch point at $x = x_b$, $y = 0$. The x axis is along the capillary axis. The angle between the x axis and the tangent vector **t** is φ, **N** is the unit normal, and s is the arc length. The branch-point angle φ_o is 60°. R_x is the loop long radius, which is the half distance between two branch points, and R_y is the loop short radius, which is the half-separation distance between the two +1/2 lines. ω_n is the normal velocity of the loop growth, ω_t is the tangent velocity, and ω_b is the branch-point velocity, respectively. At the top and the bottom of the loop $(x_0,\pm y_0)$, $\boldsymbol{\kappa} = 0$, and at the branch point $(\pm x_b,0)$, $\boldsymbol{\kappa} = \boldsymbol{\kappa}^*$.

1. Disclination line tension and bending stiffness

The Frank gradient elasticity density f for uniaxial NLCs, using the one constant approximation is [2] as follows:

$$f = \frac{K}{2}[(\nabla \cdot \mathbf{n})^2 + (\nabla \times \mathbf{n})^2]. \tag{2}$$

Minimizing the total free energy leads to the Euler-Lagrange equation: $K\nabla^2\mathbf{n} = \lambda\mathbf{n}$; K is the Frank elastic constant, and λ is the Lagrange multiplier that takes into account the unit length restriction $\mathbf{n}\cdot\mathbf{n} = 1$. The +1/2 axial disclination that forms the loop is characterized by a planar director field perpendicular to the direction of the line $\mathbf{n} = (\cos\psi, \sin\psi, 0)$. In planar polar coordinates (r,φ), a wedge disclination solution to the Euler-Lagrange equation is $\psi = m\varphi + C$, where the defect charge m is a multiple of ±1/2 and C is a constant. The occurrence of half-integer winding numbers is a result of the nematic symmetry and physical identity of the alignments **n** and −**n** [22]. By integrating Eq. (2) in a cylinder of radius R_c, one obtains the line tension γ_o(PP) of a single straight $m = +1/2$ disclination in the PP texture [21],

$$\gamma_{1/2} = \gamma_o(\mathrm{PP}) = \underbrace{\frac{\pi K}{2}\left[\ln\left(\frac{R_c^2}{2r_c y_\infty}\right)\right]}_{\gamma_{o,1/2}} + \pi\sigma_c r_c^2, \tag{3}$$

where R_c is the capillary radius, r_c is the core radius, σ_c is the core energy density that is usually assumed to be negligible in comparison to the other terms, and $2R_y$ is the distance between the two +1/2 lines defined in Fig. 4. The total line energy $\gamma_{1/2}$ (energy or length) of a curved +1/2 disclination is given by the sum of the core energy $\pi\sigma_c r_c^2$, bare line tension $\gamma_{0,1/2}$, and the bending $k_c\boldsymbol{\kappa}^2/2$ contributions [7],

$$\gamma_{1/2} = \pi\sigma_c r_c^2 + \gamma_{0,1/2} + \frac{k_c}{2}\boldsymbol{\kappa}^2, \tag{4a}$$

$$k_c = \frac{\pi K R_c^2}{\sqrt{2}}, \tag{4b}$$

where k_c is the bending modulus (energy × length) and only the leading order bending term is retained. Equation (4b) is applicable to the intermediate coarsening stage (see mode (iii) discussed above and Ref. [7]), but in the postnucleation and growth stage studied here we show below [see Eq. (31b)] that it is a function of R_y. To find the disclination shape equation, we perform the following stress balance.

2. *Disclination shape equation*

The force balance equation is written by the sum of line force $\nabla_\ell \cdot \mathbf{T}$ and the surrounding medium force [23],

$$\nabla_\ell \cdot \mathbf{T} + \oint_{\partial F} (\mathbf{N}\cdot\mathbf{T}_b)d\ell = \gamma_1\omega, \tag{5}$$

where $\mathbf{T}$ is the $+1/2$ disclination line elastic stress tensor, $\nabla_\ell(\cdot) = \mathbf{t}\,\partial(\cdot)/\partial s$ is the line gradient operator, $\mathbf{N}$ is the unit normal vector, $\mathbf{T}_b$ is the bulk stress tensor, $\mathbf{N}\cdot\mathbf{T}_b$is the elastic force acting on the disclination by the bulk, the integral is over the disclination circumference ∂F, γ_1 is the rotational viscosity, and ω is the velocity of the line. To find the $m = +1/2$ line elastic stress tensor $\mathbf{T}$, we perform a variation of the total line elastic free energy due to tangential and normal displacements and find [23,24]

$$\mathbf{T} = (\gamma_{1/2} - \mathbf{M}{:}\mathbf{b})\mathbf{I}_\ell - \frac{\partial M}{\partial s}\mathbf{tN}, \tag{6}$$

where $\gamma_{1/2}\mathbf{I}_\ell$ is the thermodynamic tension stress analogous to three-dimensional pressure. The elastic line stress $\mathbf{T}$ has a mechanical contribution ($-\mathbf{M}{:}\mathbf{b}$) since there can be no bending without tension; here $\mathbf{b}$ is the line curvature tensor given by $\mathbf{b} = \boldsymbol{\kappa}\ \mathbf{I}_\ell$. The last terms in Eq. (6) are the bending stresses that arise under curvature gradients ($\partial\boldsymbol{\kappa}/\partial s \neq 0$). The scalar moment M, line moment tensor $\mathbf{M}$, and line elastic stress tensor $\mathbf{T}$ are as follows:

$$M = k_c\boldsymbol{\kappa}, \tag{7a}$$

$$\mathbf{M} = k_c\boldsymbol{\kappa}\mathbf{I}_\ell, \tag{7b}$$

$$\mathbf{T}^e = \left(\gamma_{o,1/2} - \frac{k_c}{2}\boldsymbol{\kappa}^2\right)\mathbf{I}_\ell - k_c\frac{\partial\boldsymbol{\kappa}}{\partial s}\mathbf{tN}. \tag{7c}$$

Assuming that bulk dissipation is generated by bulk forces:$\oint_{\partial F}(\mathbf{N}\cdot\mathbf{T}_b)d\ell = \gamma_1\omega$ and placing Eqs. (4) and (7) into (6), we find the disclination shape equation, known as *nematic elastica*, as a balance between tension and bending forces,

$$\underbrace{\gamma_{0,1/2}\boldsymbol{\kappa}}_{\text{tension}} - \underbrace{k_c\left(\boldsymbol{\kappa}_{ss} + \frac{\boldsymbol{\kappa}^3}{2}\right)}_{\text{bending}} = 0. \tag{8}$$

The diffusive term $k_c\boldsymbol{\kappa}_{ss} = k_c\partial^2\boldsymbol{\kappa}/\partial s^2$ and the nonlinearity $k_c\boldsymbol{\kappa}^3/2$ arise due to the bending stresses in Eq. (5). We assume that $\gamma_{0,1/2} + \mu\ \partial\boldsymbol{\kappa}/\partial t \approx \gamma_{0,1/2}$ and the line viscosity term is negligible (see Appendix C). Equation (8) is a steady nonlinear reaction-diffusion equation in which the time dependency of the curvature $\boldsymbol{\kappa}(s)$ that describes loop growth enters through transient boundary conditions at the moving branch point $[x_b(t),0]$ and at the $[0,R_y(t)]$.

C. Disclination loop shape equation

For simplicity we use the one loop quadrant. For the selected fixed (x,y) coordinates, the amplitude of the loop corresponds to zero arch length ($s = 0$), whereas the branch point corresponds to $S^*(t)$. To derive the loop shape equation we subject Eq. (8) to time-dependent curvature boundary conditions,

$$s = S^*(t), \quad \boldsymbol{\kappa} = \boldsymbol{\kappa}^*(t) = d\phi/ds|_{S^*(t)}, \tag{9a}$$

$$s = 0, \quad \boldsymbol{\kappa} = 0, \tag{9b}$$

where S^* and $\boldsymbol{\kappa}^*$ are functions of time. The two important parameters in Eqs. (8) and (9) that will affect the shape of the loop are the ratio of the tension to bending stiffness ($a = \gamma/k_c[=]\text{length}^{-2}$) and the branch-point curvature ($\boldsymbol{\kappa}^*$), which are functions of capillary size [7].

1. *Disclination space loop*

In the selected quadrant the space loop is given by the evolving space curve $[x(t),y(t)]$. From the Fresnel integrals [25] we have

$$x(s,a,\boldsymbol{\kappa}^*,t) = \int_0^{S^*(t)} \cos\left[\int_0^{s'} \boldsymbol{\kappa}(s'',a,\boldsymbol{\kappa}^*)ds''\right]ds', \tag{10}$$

$$y(s,a,\boldsymbol{\kappa}^*,t) = \int_0^{S^*(t)} \sin\left[\int_0^{s'} \boldsymbol{\kappa}(s'',a,\boldsymbol{\kappa}^*)ds''\right]ds', \tag{11}$$

where a is the tension to the bending ratio: $\gamma_{0,1/2}/k_c$. The boundary conditions written in terms of y and x are as follows:

$$x = 0, \quad y = y_0(t), \tag{12a}$$

$$x = x_b(t), \tag{12b}$$

$$\left.\frac{dy}{dx}\right|_{x_b} = \tan(60^\circ), \tag{12c}$$

where $x_b(t)$ is the branch-point position on the x axis and $y_0(t) = R_y$ is the loop height. Corresponding boundary conditions can be defined for the other loop quadrants. Equation (12) assumes a constant branch angle $\theta_b = 60^\circ$, extensively discussed previously [7].

Equations (8) and (10)–(12) are solved simultaneously in the domain $x_{b-}(t) \leqslant x \leqslant x_{b+}(t)$.

2. *Loop growth laws*

The time-dependent boundary conditions [Eq. (12)] require loop growth expressions. Growth laws of +1/2 loop growth attached to +1 disclinations under confinement have not been established. Nevertheless by using +1 disclination splitting into two +1/2 lines under capillary confinement (SD mode) it was found [21] that in the intermediate stage of the PR → PP transition the defect-defect distance ℓ_{defect} is described by a

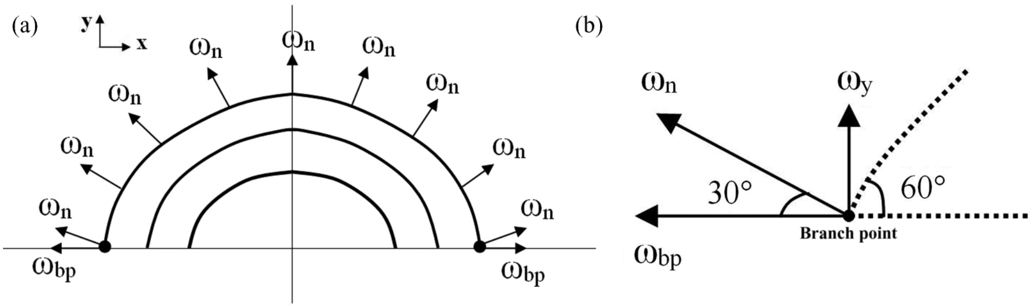

FIG. 5. (a) Schematic of the system of parallel curves created as a result of the disclination loops' growth process. The branch-point angle remains unchanged during the evolution, so the normal velocity ω_n is uniform along the curve; (b) the normal velocity at the branch point. The fact that a 60° angle at the branch points leads to a relation between the axial and the vertical velocities [Eq. (17)], which helps us to predict one from another.

power law of the type,

$$\ell_{\text{defect}} = At^n, \tag{13}$$

where $n \approx 0.2$. Assuming an anisotropic rate of expansions for the loop, the previous scaling yields

$$R_x(t) = A_x t^{0.2}, \tag{14a}$$

$$R_y(t) = A_y t^{0.2}, \tag{14b}$$

and the anisotropy ε of the loop is a constant,

$$\varepsilon = \frac{R_y(t)}{R_x(t)} = \frac{A_y}{A_x} \tag{15}$$

In this paper we use as characteristic values $A_x = 22.5$, $A_y = 15$, so the ratio $\varepsilon = 0.667$ is close to what has been observed experimentally [8].

D. Kinematic characterization

During loop growth the normal velocity $\omega_n(s,t)$ is a function of arc length and time [see Fig. 5(a) below for details]. Figure 5(b) shows the normal, axial, and vertical velocities at the branch point. At each point of the curves, the normal velocity is a vector sum of the axial and vertical velocities. The axial velocity at the branch point is called branch-point velocity. Using the previously established [7–9] constant branch angle, the axial and vertical BP velocities are as follows:

$$\omega_y(t)|_{\text{BP}} = \omega_n(t)|_{\text{BP}} \sin(30^\circ), \tag{16a}$$

$$\omega_x(t)|_{\text{BP}} = \omega_n(t)|_{\text{BP}} \cos(30^\circ). \tag{16b}$$

Hence kinematic compatibility leads to

$$\frac{\omega_y(t)|_{\text{BP}}}{\omega_x(t)|_{\text{BP}}} = \tan(30^\circ). \tag{17}$$

In terms of growth velocities we have a slowdown of exponents close to -1,

$$\omega_x(t)|_{\text{BP}} = 0.2 A_x t^{-0.8}, \quad \omega_y(t)|_{s=0} = 0.2 A_y t^{-0.8}. \tag{18}$$

To find the normal velocity $\omega_n(s,t)$ along the disclination curve we can use the transport theorem for a closed loop [23],

$$\Delta(t) = \frac{dL}{L\,dt} = -\frac{1}{L}\int_0^{S^*(t)} \boldsymbol{\kappa}(s,t)\omega_n(s,t)ds, \tag{19}$$

where $L(t)$ is the total length of the disclination curve and $\Delta(t)$ is the dilation of the loop [25,26]. Hence the time-dependent dilation $\Delta(t)$ encapsulates the geometry $[\boldsymbol{\kappa}(s,t)]$ and kinematics $[\omega_n(s,t)]$ of the growing disclination loop.

E. Computational methods

To find the shape of the evolving loop under micron-range confinement we solve Eqs. (8), (10), and (11), subjected to boundary conditions [Eq. (12)] using a standard iterative method; see Appendix A. The analytical solution of Eq. (8) presented in Ref. [7] is used to estimate initial values for arc length. The initial time is $t_o = 100$ s when the loop shape is a quartic $y = \pm(-9 \times 10^{-7}x^4 - 0.0065x^2 + 37.17)$; all distances used in this paper are in microns. The time step to describe growth is 10 s, and the final time is 1400 s when R_y becomes close to the saturation value $0.665R_c$ [7]. The capillary radius is $R_c = 100\ \mu$m, and the branch point angle is fixed at 60° for all cases (see Appendix B).

III. RESULTS AND DISCUSSION

We recall that starred values refer to values at the branch points. Unless explicitly mentioned due to the symmetries of the loop and for brevity, we mainly show results for one quadrant.

A. Curvature $\boldsymbol{\kappa}(s)$

The evolutions of the $+1/2$ disclination loop are characterized in terms of: (a) the curvature $\boldsymbol{\kappa}(s)$, (b) the total arc length $S^*(t)$ and the branch-point curvature $\boldsymbol{\kappa}^*(t)$, and (c) the total loop curvature $\boldsymbol{\kappa}_t(t)$.

1. Curvature $\boldsymbol{\kappa}(s)$

Figure 6(a) shows the curvature $\boldsymbol{\kappa}(s)$ as a function of arc length for $t = 100, 700,$ and 1400 s for $0 < x < x_b$ and the fourth quadrant of the disclination curve. The curvature increases exponentially as the branch point is reached, and loop expansion decreases $\boldsymbol{\kappa}^*$ [see also Fig. 6(b)]. Complex spatiotemporal changes in the curvature reflect the tension-bending elasticity under growth conditions. Figure 6(b) shows the exponential-like decay of the diffusion-to-nonlinear bending ratio $2\boldsymbol{\kappa}_{\text{ss}}/\boldsymbol{\kappa}^3$ as a function of arc length for $t = 100$, 700, and 1400 s. The figure demonstrates that the relative importance of bending

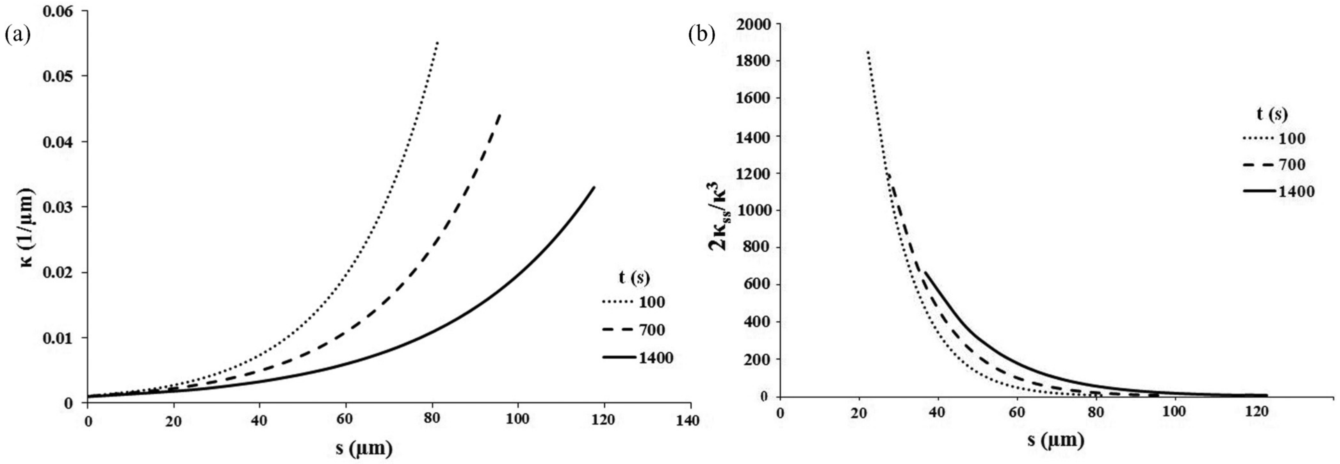

FIG. 6. (a) Effect of time on curvature $\kappa(s)$ as a function of arc length. For the later time, the final curvature κ^* is smaller; (b) the diffusion to nonlinear bending ratio $2\kappa_{ss}/\kappa^3$ as a function of arc length for $t = 100$, 700, and 1400 s. This ratio increases over time.

stress (diffusion term κ_{ss}) to tension stress (cubic term κ^3) is maximal at $x = 0$ and vanishes at the branch point.

2. *Total arc length $S^*(t)$*

Figure 6(a) shows the final arc length $S^*(t)$ as a function of time. The increases from 82.85 μm at $t = 100$ s to 126.34 μm at $t = 1400$ s are associated with the loop expansion. On the other hand Fig. 7(b) shows that as the loop grows, the branch-point curvature decreases. The data shown in Figs. 7(a) and 7(b) can be collapsed into power laws,

$$S^* = 43.5t^{0.15}, \tag{20a}$$

$$\kappa^* = 0.14t^{-0.19}. \tag{20b}$$

Comparing with Eq. (13) we retrieve the expected results:$S^* \approx o(R_x + R_y)$; $\kappa^* \approx o(R_x + R_y)^{-1}$, the latter is shown in Fig. 14.

The dimensionless number $P = S^*\kappa^*$, which is the ratio of loop growth to maximum loop curvature, shown in Fig. 7(c), is a weak function of time as per Eq. (20) and higher than that for circular growth ($P \geqslant \pi R/R = 3.14$).

3. *Total curvature κ_t*

Figure 7(d) shows the total curvature κ_t for a quarter loop as a function of time. The total curvature κ_t is the subtended angle ψ(rad) of the disclination arc (for a circle of radius R, the subtended angle is as follows:$\psi = S^*/R$) and is a function of S^* as well as $\kappa(s)$. The subtended angles ψ(rad) are essentially constant because of a constant branch angle [27],

$$\kappa_t = \int_{\text{branch point}}^{\kappa=0\text{ point}} \frac{\partial\theta}{\partial s} ds = \frac{\pi}{2} - \frac{\pi}{6}, \tag{21}$$

so the total curvature for all cases should be $\pi/3$. The essentially negligible temporal decrease in $\kappa_t$shown in Fig. 7(b) is due to unavoidable but negligible computational errors.

B. Disclination curve $y(x)$

Figure 8(a) shows representative disclination curves $y(x)$ for $t = 100$, 700, and 1400 s. At $t = 100$ s, $R_x = 52.77$ and $R_y = 37.67$ μm which increase to $R_x = 97.22$ and $R_y = 65.87$ μm at $t = 1400$ s. The disclination curve that satisfies is essentially a quartic,

$$y = \pm\left[-\left(\frac{9\times10^{-7}}{t^{0.5}}\right)x^4 - \left(\frac{0.0075}{t^{0.03}}\right)x^2 + R_y(t)\right], \tag{22}$$

where $R_y(t) = 15t^{0.2}$; the quartic fit has a standard deviation of 0.97.

Figure 8(b) shows the changes in the slope of the disclination curves over time for $0 \leqslant x \leqslant x_{b+}(t)$. The funnel shape reflects the time-invariant fact that the curvature vanishes as we approach $x = 0$.

C. Kinematics

Figure 9(a) shows the growth velocities [$\omega_x(y=0)$, $\omega_y(x=0)$,$\omega_x(x=x_b)$]. These velocities show a power law decrease followed by a terminal velocity. This regime signals proximity to the transition intermediate stage of coarsening characterized by $R_y = 0.66R_c$ and $\omega_x(x = x_{BP}) = \omega_t$ and $\omega_y(x=0) = 0$, where ω_t is a terminal velocity. At $t = 1400$ s, the R_y reaches the saturation value ($y_\infty = 0.66R_c$) [7–9] at which the terminal velocity will be around $\omega_t = 0.016$ μm/s. This value is rationalized by this fact that the branch points move slowly, which does not affect the disclination curve shape. The ordering of the growth velocities follows from kinematic compatibility [Eq. (17)] and growth kinetics [Eq. (18)]:

$$\begin{aligned}\omega_n(t)|_{\mathrm{BP}} &= \frac{\omega_x(t)|_{\mathrm{BP}}}{\cos(30^\circ)} > \omega_x(t)\Big|_{\mathrm{BP}}\\ &= 5.19t^{-0.8} > \omega_y(t)|_{s=0} = 3t^{-0.8}.\end{aligned} \tag{23}$$

Figure 9(b) shows the normal velocity $\omega_n(s,t)$ as a function of arc length computed from Eqs. (18). The time functionality of the normal velocity $\omega_n(s,t)$ is essentially homogeneous over the disclination curve as per Eqs. (14), the upper and lower

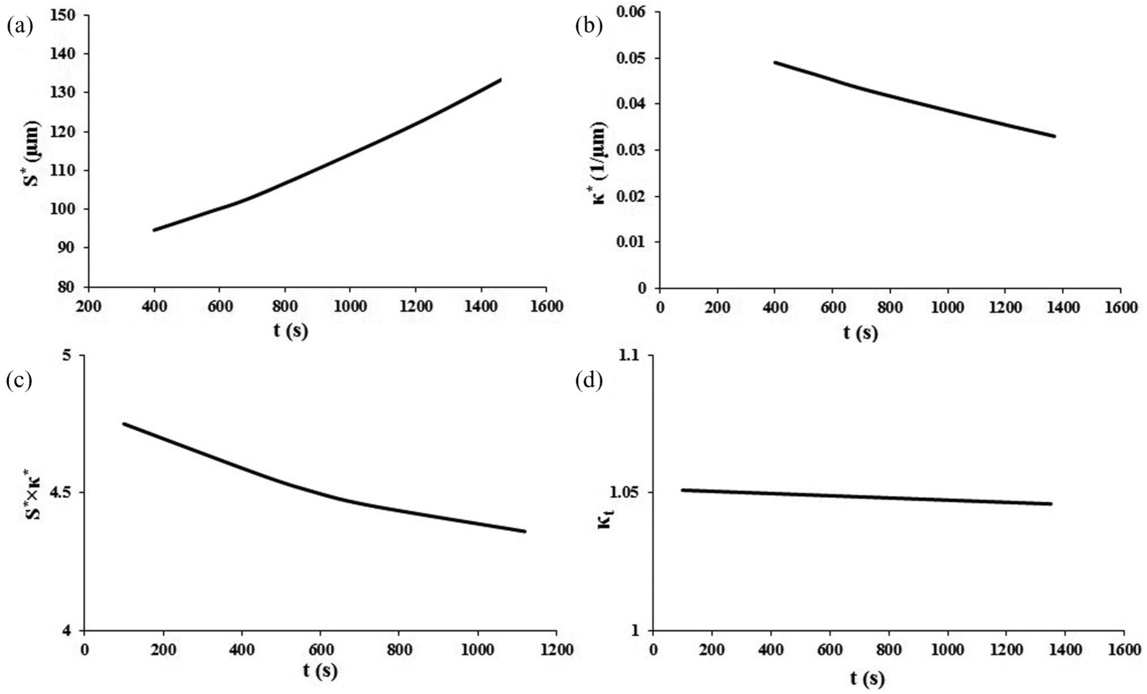

FIG. 7. (a) The final arc length as a function of time. S^* increases with time; (b) the branch-point curvature as a function of time. $\boldsymbol{\kappa}^*$ decreases with time; (c) the dimensionless number $P = S^*\boldsymbol{\kappa}^*$ as a function of time. This number is larger for smaller loops than for larger loops; (d) the total curvature for a quarter loop as a function of time. The total curvature is independent of the time.

limits decrease as $t^{-0.8}$,

$$\underbrace{\omega_n(s=S^*,t)|_{\mathrm{BP}}=\frac{5.5}{t^{0.8}}}_{\text{branch point normal velcity}} > \omega_n(s,t) > \underbrace{\omega_n(s=0,t)|_{x=0}=\frac{3}{t^{0.8}}}_{\text{vertical velocity at } x=0}. \tag{24}$$

Figure 10(a) shows the loop dilation $\Delta(t) = (dL/dt)/L$ as a function of time. The power law for dilation is

$$\Delta = 0.15t^{-1} \tag{25}$$

and follows the growth scaling:

$$\frac{dL}{dt} = 6.5t^{-0.85} \tag{26}$$

Figure 10(b) shows the computed stiffness ratio $a = \gamma_{0,1/2}/k_c$ as a function of R_y. We recall that $a(t) = \gamma_{0,1/2}/k_c$ is not a constant material property, but it depends on time as k_c depends on the confinement (see Fig. 13). The present stiffness ratio data in the nucleation and growth mode can be

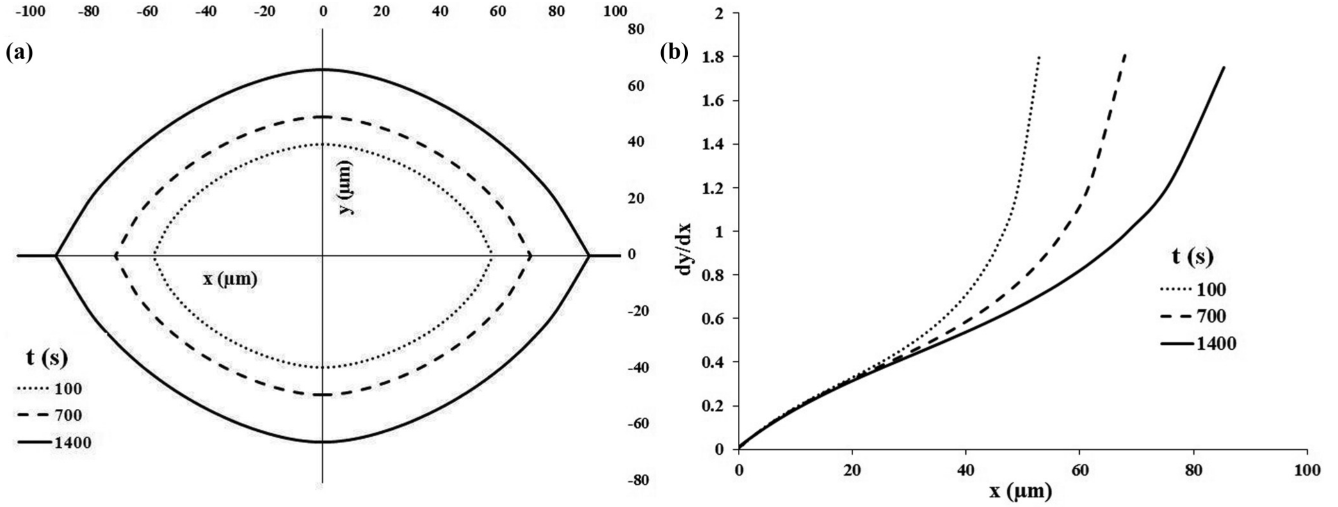

FIG. 8. (a) The disclination curves as a function of time. The size of the loops increases over time; (b) the slope of the disclination curves dy/dx for $t = 100$, 700, and 1400 s. The rate of change is faster for the smaller loops.

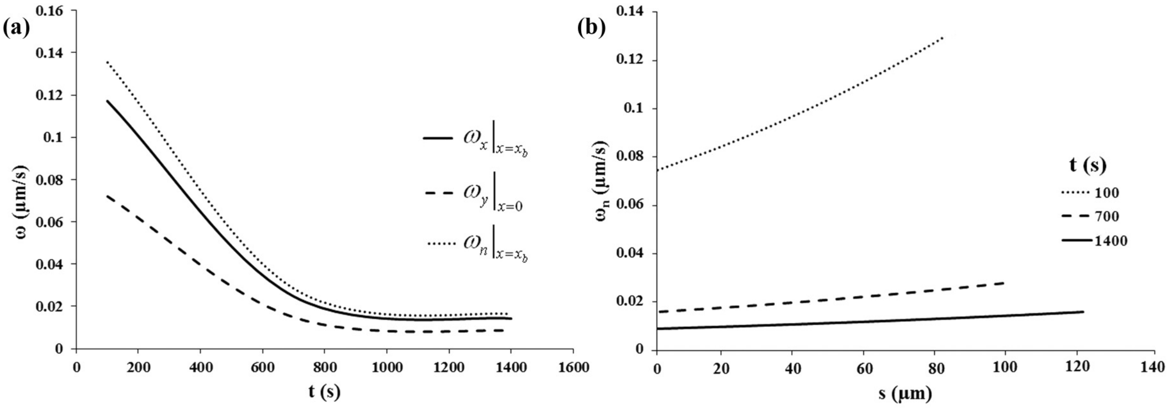

FIG. 9. (a) The growth velocity in the x and y directions and the normal velocity at the branch point as functions of time. These velocities decrease until they reach a terminal velocity; (b) normal velocity as a function of the arc length for $t = 100$, 700, and 1400 s. Over time, the normal velocity becomes a weak function of arc length.

collapsed into the power law,

$$a(t) = \frac{\gamma_{0,1/2}}{k_c} \equiv \frac{1}{(l_M)^2} \approx \frac{4}{R_y^2(t)} \tag{27}$$

where l_M is the material length scale (see also Appendix B). Equation (27) simply states that the material length scale l_M is one half of the geometric length scale R_y: $l_M = R_y/2$. In the coarsening mode we found [7] that the material length scale is $l_M = R_y/3$. Since the limiting value of R_y is as follows: $R_y(t \to \infty) = R_c/3$ we find that the long term time limit of Eq. (27) is consistent with our previous result [7] since

$$\lim_{t\to\infty} R_y \approx \sqrt{\frac{4}{9}} R_c = 0.66 R_c. \tag{28}$$

D. Disclination energy

The total energy of a $+1/2$ disclination loop is the sum of total tension and total bending contributions,

$$E_T = E_b + E_t, \tag{29}$$

where E_b and E_t are the total bending and total tension energy defined (for a loop quadrant) by

$$E_t(t) = \int_0^{S^*(t)} \gamma_{o,1/2}(s,t)ds, \tag{30a}$$

$$E_b(t) = \int_0^{S^*(t)} \left(\frac{k_c}{2}\kappa^2(s,t)\right)ds, \tag{30b}$$

where according to Eqs. (3), (4), and (28) the time-dependent tension and bending stiffness of a growing loop in terms of the semiaxes $R_y(t)$ are well approximated by

$$\gamma_{o,1/2}(t) = \frac{\pi K}{2} \ln\left(\frac{9R_y(t)}{8r_c}\right), \tag{31a}$$

$$k_c(t) = \frac{9\pi K R_y^2(t)}{4\sqrt{2}}. \tag{31b}$$

We note that Eqs. (31) used to calculate the total energy E_t are consistent with Eq. (27) since

$$a(t) = \frac{2\sqrt{2}\ln\left(\frac{9R_y(t)}{8r_c}\right)}{9R_y^2(t)} \approx \frac{4}{R_y^2(t)} \tag{32}$$

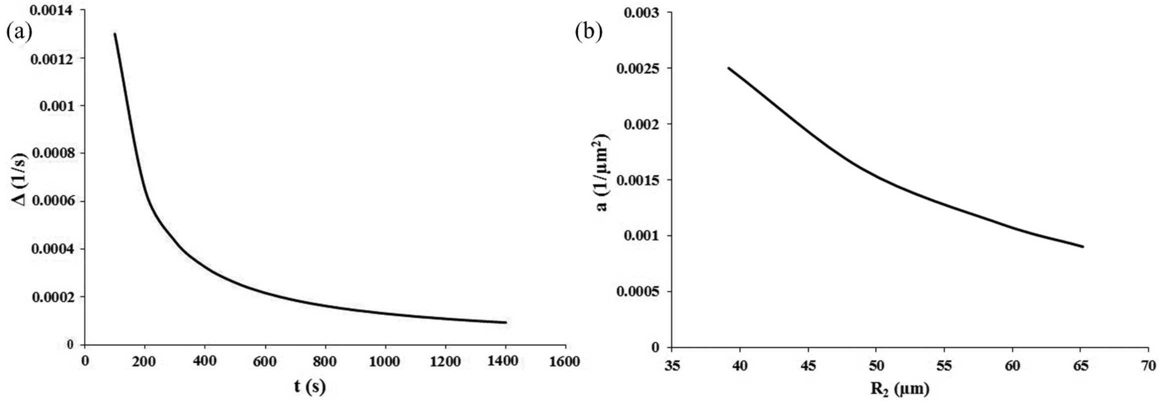

FIG. 10. (a) The loop length dilation Δ as a function of time. The loop growth rate decreases as $t^{-0.85}$; (b) the stiffness ratio $a(t) = \gamma_{0,1/2}/k$ as a function of the loop short radius R_y. When the loop size increases, $a(t) = \gamma_{0,1/2}/k$ decreases as $4/R_y^2$.

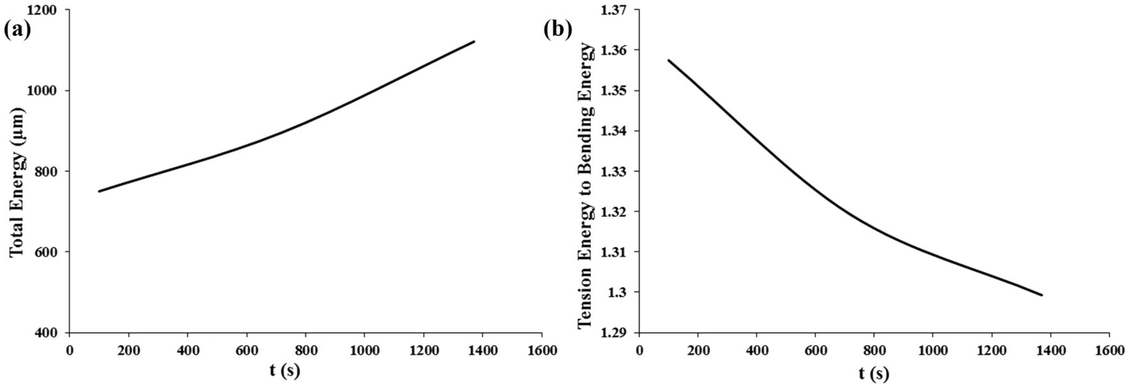

FIG. 11. (a) Scaled total disclination line energy $E_{\mathrm{T}}/\pi K$ as a function of time; (b) the ratio of the total tension energy per the total bending energy length as a function of t.

Figure 11(a) shows the scaled total energy $E_{\mathrm{T}}/\pi K$ as a function of time (single loop quadrant). The power law is as follows:$E_t = 386t^{0.14}$. The scaled energy increases since S^* increases and the line tension increases; the term $k_c\boldsymbol{\kappa}^2$ is essentially time independent.

Figure 11(b) shows the ratio of the tension energy to the bending energy as a function of time. According to Eqs. (30), E_{T} is a function of $S^*(t)$ and the bending energy density, which is the product of the bending stiffness times the curvature. Curvature decreases over time, but the bending stiffness increases as a result of increasing in loop size, so this ratio decreases slightly over time, from 1.358 at $t = 100$ s to 1.281 at $t = 1400$ s. At the branch point x_b, the energy ratio is close to 1.25.

Figure 12(a) shows the scaled total energy $E_{\mathrm{T}}/\pi K$ (μm) as a function of the branch-point curvature $\boldsymbol{\kappa}^*$. The smaller loop radius is accommodated by a larger and energetically less costly curvature. By increasing the loop radius, the branch point curvature $\boldsymbol{\kappa}^*$ decreases, but the scaled total energy $E_{\mathrm{T}}/\pi K$ increases. Figure 12(b) integrates schematically the effects of time on the disclination loop found from simulations (Figs. 6–8 and 10). In the early stage, small loops lead to high curvature and low total energy, and as time elapses the length S^*, tension E_t, and bending E_b energies increase while the branch point curvature $\boldsymbol{\kappa}^*$ and normal velocity ω_n decrease.

IV. CONCLUSIONS

This paper presents theory and simulation of the postnucleation and growth mode of the transformation of a nematic liquid crystal planar radial texture with one axial $+1$ singular disclination into a planar polar texture with two $+1/2$ singular disclinations that occurs in a capillary whose surfaces impose homeotropic anchoring. In the initial stages an array of $+1/2$ loops nucleate on the preexiting $+1$ line and slowly grow by an elastic driving force that is generated by the elimination of the director radial splay. Each $+1/2$ loop is connected to the $+1$ line by two branch points, and the elliptical cusped loop grows with subdiffusive kinetics($R_{\mathrm{loop}} \approx t^n, n < 1/2$). We presented, solved, and characterized a model based on the nematic elastica that incorporates tension and bending stiffness. The cusped elliptical loop geometry is the result of strong bending at the two branch points which results in an exponential decrease in curvature when moving away from these cusps. The subdiffusive loop growth is reflected in the total length, curvature, and dilation. The total energy of the

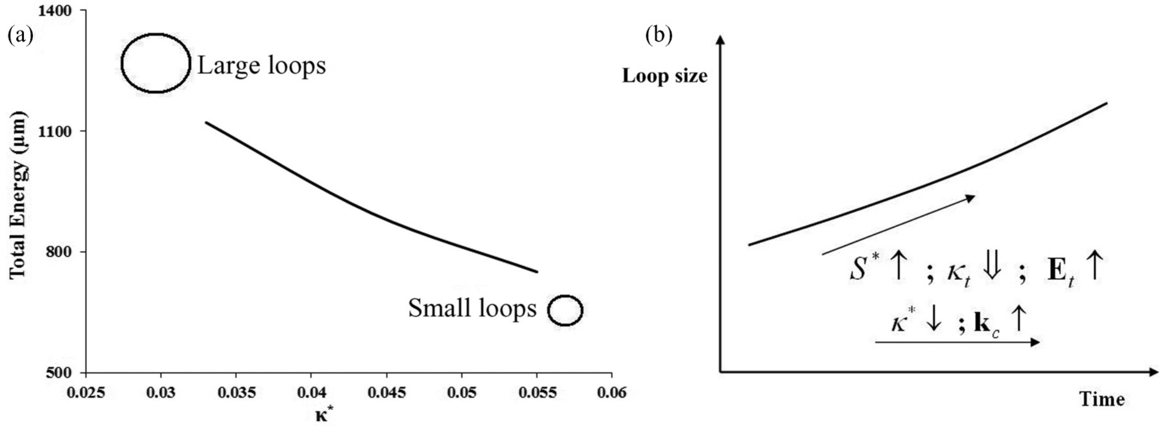

FIG. 12. (a) The scaled total energy $E_{\mathrm{T}}/\pi K$ as a function of the branch-point curvature $\boldsymbol{\kappa}^*$. Increasing the loop size decreases the curvature and increases the total energy; (b) parametric plane indicating the total energy E_{T} and final arc length S^* of the disclination loop as a function of loop size and time. The loop size increases over time and leads to significant changes in the total energy E_{T} and final arc length S^*. The growth velocity decreases over time until reaching a terminal velocity.

loop increases with decreasing the branch-point curvature as the length increase effect is larger than the curvature decrease. We demonstrated that when the branch angle is close to $\pi/3$, the material length scale l_M is one half of the loop short axes.

The introduction of a nematic elastica model to solve texture transformations under confinement can in the future be extended to nonplanar disclinations where disclination torsion arises. The modeling predictions from the nematic elastica model enhance the current fundamental understanding of the defect physics of liquid crystals.

ACKNOWLEDGMENTS

This work was supported a grant from the U.S. Office of Basic Energy Sciences, Department of Energy; Grant No. DE-SC0001412.

APPENDIX A: NUMERICAL METHODS

To find the evolving loop shape $y(x,t)$ we solve Eqs. (8), (10), and (11) using time-dependent boundary conditions subjected to constraints given by Eq. (12). The computational domain is discretized into $n = 100$ nodes. To find the final curvature ($\boldsymbol{\kappa}^*$) and initial values for the bending to tension ratio (a) we use the following initial guess as per our previous paper [7]:

$$\boldsymbol{\kappa}^* = \frac{10}{3y^*(t)}, \quad a = \left(\frac{3}{y^*(t)}\right)^2. \tag{A1}$$

The boundary conditions are as follows:

$$y(1) = y^*(t), \quad x(1) = 0, \quad \boldsymbol{\kappa}(1) = 0, \tag{A2a}$$

$$y(n) = 0, \quad x(n) = x_b(t), \quad \boldsymbol{\kappa}(n) = \boldsymbol{\kappa}^*. \tag{A2b}$$

From our previous papers [7–9] the analytical solution for the shape Eq. (8) is given by

$$\begin{aligned} \boldsymbol{\kappa} &= \pm 2\sqrt{a}\left\{\frac{-2Ce^{-\sqrt{a}s}}{\left[C^2\left(e^{-\sqrt{a}s}\right)^2 + 1\right]}\right\}, \\ C &= \frac{\sqrt{4a - \boldsymbol{\kappa}_o^2} - \sqrt{4a}}{\boldsymbol{\kappa}_o}, \end{aligned} \tag{A3}$$

where $\boldsymbol{\kappa}(s = 0,t) = \boldsymbol{\kappa}_o$. To find the arc length at the ith node we use Eq. (A3),

$$s(i) = 2\sqrt{a}\ln\left(\frac{1}{C - \boldsymbol{\kappa}(i) - \frac{2\sqrt{a}}{\boldsymbol{\kappa}(i)}}\right), \tag{A4}$$

in a loop for $i \geq 2$. Then we find $x(i)$ and $y(i)$,

$$x(i) = \int_{s(1)}^{s(i)} \cos(\theta)ds + x(1), \tag{A5}$$

$$y(i) = \int_{s(1)}^{s(i)} \sin(\theta)ds + y(1), \tag{A6}$$

where φ is the tangent angle defined as follows:

$$\varphi(i) = \alpha + \frac{\pi}{2} + \int_{s(n)}^{s(i)} \boldsymbol{\kappa}(i)ds. \tag{A7}$$

The value of $s(n)$ is found from

$$at\ (s = s^*)\colon \int_{s(n)}^{0} \boldsymbol{\kappa}(i)ds = \frac{\pi}{3} - \frac{\pi}{2}. \tag{A8}$$

The slope dy/dx at the branch point must satisfy

$$\begin{aligned} &\frac{dy}{dx}[at\ (s = S^*)]\colon \tan(60^\circ), \\ &y(n) = [x(n) - x(n-1)]\tan(60^\circ) + y(n-1). \end{aligned} \tag{A9}$$

If the branch angle is essentially equal to 60° (error $<$ 0.01), the initial guess for $\boldsymbol{\kappa}^*$ and a is acceptable, otherwise we redo the loop calculation. After each converged step, time is updated in the forward-marching scheme,

$$t = t + h \tag{A10}$$

where h is the time step.

APPENDIX B: BRANCH POINT ANGLE

In this Appendix we establish the origin of the branch-point angle $\varphi_o = 60^\circ$ shown in Fig. 4. As the loop grows, both tension and bending stiffness change as indicated in Eqs. (27) and (31). The ratio $a = \gamma_{0,1/2}/k_c$ decreases with increasing R_y, and hence the bending stiffness increases [Eq. (32)]. As the material parameter $a = \gamma_{0,1/2}/k_c$ evolves, the geometry also evolves, increasing the total loop length and decreasing the total loop curvature. The imposed constant branch angle is the condition that leads to the balance between these two effects.

Figure 13 shows the branch-point angle as a function of the loop radius R_y for several values of $a = \gamma_{0,1/2}/k_c$. The lines cross the 60° branch angle value at R_y values that satisfy Eq. (32). We conclude that the 60° branch angle constraint simply indicates that the material length scale is one half of the geometric scale R_y: $1/\sqrt{a(t)} \approx R_y(t)/2$. This length increases over time as shown in Fig. 14. This figure also shows that the inverse of the curvature at the branch point $1/\boldsymbol{\kappa}^*$ scales linearly with R_y. Figure 14 demonstrates that the branch angle $\varphi_o =$ 60° is due to the consistency of the three length scales: R_y, $1/\boldsymbol{\kappa}^*$, and l_M.

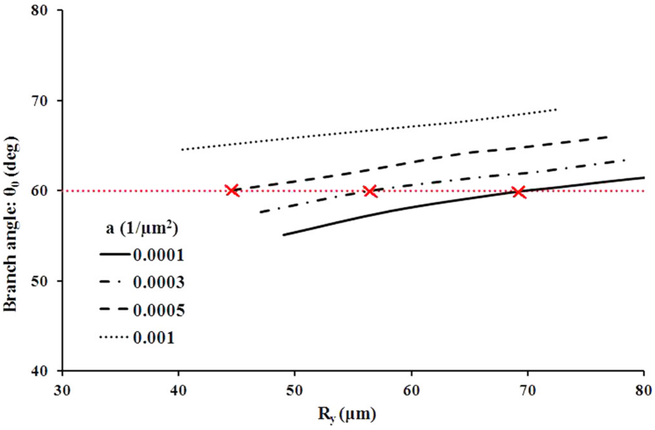

FIG. 13. (Color online) Branch-point angle as a function of the loop short radius under capillary confinement, computed using a fixed the tension or bending stiffness ratio $a = \gamma_{0,1/2}/k_c$ and changing the final curvature $\boldsymbol{\kappa}^*$.

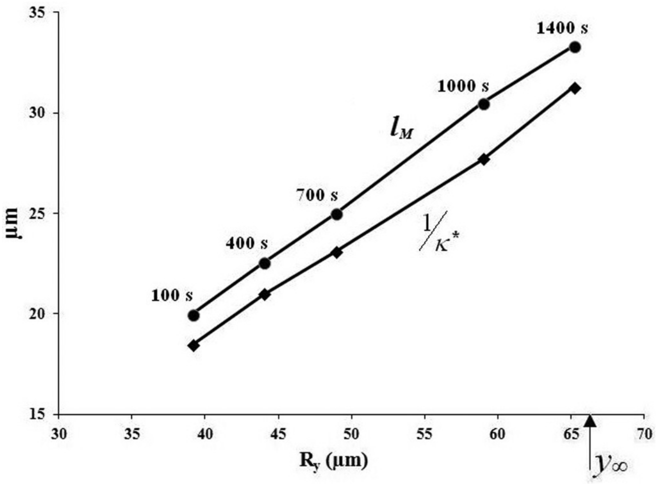

FIG. 14. Material length scale l_M and the reverse of the branch-point curvature as a function of R_y for different times. The two length scales are linear functions of R_y and are of the same order of magnitude.

APPENDIX C: VISCOUS TERM

The purpose of Appendix C is to demonstrate that line viscous dissipation is negligible. The line viscosity is as follows:

$$\mu = \pi r_c^2 \gamma_1 \tag{C1}$$

where γ_1 is the rotational viscosity and r_c is the defect core radius. Next we compare the line tension force $\gamma_{0,1/2}\boldsymbol{\kappa}$ with the viscous force $\mu\ \partial\boldsymbol{\kappa}/\partial t$. The values of the line tension and rotational viscosity can be estimated by studying the uniform motion of the branch points. The branch-point velocity can be estimated from the dR_x/dt. Assuming that the Frank elastic constant is $K \approx 10$ pN, which is a measured value for a well-studied chromonic LC disodium cromolyn glycated by dynamic light scattering [28], we estimate that the rotational viscosity is $\gamma_1 \approx 5$ Pa s. According to Eq. (4b), the bending modulus is $k_c \approx 2.5 \times 10^{-7}$ pN m^2, and using Fig. 13, the bare line tension is estimated to be $\gamma_0 \approx 200$ pN. Figure 15 shows the ratio of the line tension force ($\gamma_{0,1/2}\boldsymbol{\kappa}$) to the viscous force $\mu\partial\boldsymbol{\kappa}/\partial t$ as a function of time. It can be seen even for small loops that the viscous term is negligible.

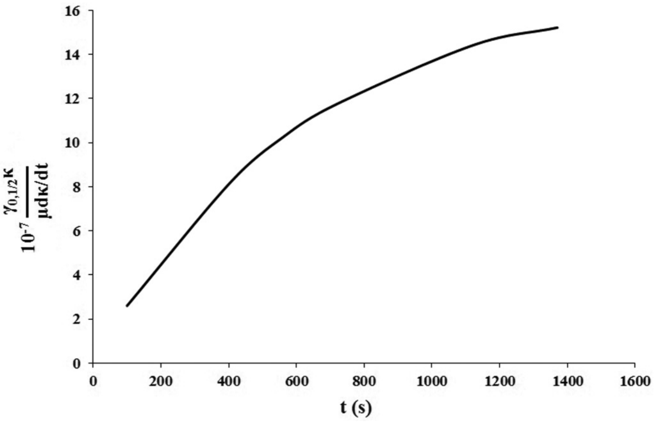

FIG. 15. The ratio of tension forces to the viscous force. It can be seen that the viscous force is negligible compared to the line tension force.

---

[1] M. Kleman and O. D. Lavrentovich, *Soft Matter Physics* (Springer-Verlag, New York, 2003).
[2] P. G. de Gennes, *The Physics of Liquid Crystals* (Oxford University Press, New York, 1995).
[3] E. G. Virga, *Variational Theories for Liquid Crystals* (Chapman & Hall, London, 1994).
[4] I. W. Stewart, *The Static and Dynamic Continuum Theory of Liquid Crystals: A Mathematical Introduction* (Taylor & Francis, New York, 2004).
[5] *Defects in Liquid Crystals: Computer Simulations, Theory and Experiments*, edited by O. D. Lavrentovich, P. Pasini, C. Zannoni, and S. Žumer, *Nato Science Series, II. Mathematics, Physics and Chemistry* Vol. 43 (Kluwer Academic, The Netherlands, 2001).
[6] *Liquid Crystals in Complex Geometries: Formed by Polymer and Porous Networks*, edited by G. P. Crawford and S. Zumer (Taylor & Francis, London, 1996).
[7] A. Shams, X. Yao, J. O. Park, M. Srinivasarao, and A. D. Rey, Soft Matter **8**, 11135 (2012).
[8] A. Shams, X. Yao, J. O. Park, M. Srinivasarao, and A. D. Rey, *Disclination Shape Analysis for Nematic Liquid Crystals under Micron-range Capillary Confinement, MRS Online Proceedings Library* (Cambridge University Press, Cambridge, 2013), Vol. 1526; X. Yao, A. D. Rey, J. O. Park, and M. Srinivasarao, *Lyotropic Chromonic Liquid Crystals in the Biphasic Region, APS March Meeting Processing, Boston, 2012* (APS, College Park, MD, 2012), Vol. 57.
[9] A. Shams, X. Yao, J. O. Park, M. Srinivasarao, and A. D. Rey, Soft Matter **10**, 3245 (2014).
[10] A. D. Rey, Soft Matter **6**, 3402 (2010); A. D. Rey and E. E. Herrera Valencia, *ibid.* **10**, 1611 (2014); B. Wincure and A. D. Rey, Liq. Cryst. **34**, 1397 (2007); Nano Lett. **7**, 1474 (2007); Discrete Continuous Dyn. Syst., Ser. B **8**, 623 (2007); Continuous Mech. Thermodyn. **19**, 37 (2007); J. Chem. Phys. **124**, 244902 (2006).
[11] B. T. Gettelfinger, J. A. Moreno-Razo, G. M. Koenig, Jr., J. P. Hernández-Ortiz, N. L. Abbott, and J. J. de Pablo, Soft Matter **6**, 896 (2010).
[12] M. Srinivasarao, in *Liquid Crystals in the Nineties and Beyond*, edited by S. Kumar (World Scientific, Singapore, 1995), pp. 18,19, 377–434.
[13] F. R. Hung, Phys. Rev. E **79**, 021705 (2009).
[14] A. D. Rey, Macromol. Theory Simul. **11**, 944 (2002).
[15] A.-G. Cheong, A. D. Rey, and P. T. Mather, Phys. Rev. E **64**, 041701 (2001).
[16] A. D. Rey, Langmuir **19**, 3677 (2003).
[17] A. D. Rey, Soft Matter **3**, 1349 (2007).
[18] A. D. Rey, Rheol. Rev. **2008**, 71 (2009).

[19] Y. K. Kim, S. V. Shiyanovskii, and O. D. Lavrentovich, J. Phys.: Condens. Matter **25**, 404202 (2013).

[20] G. De Luca and A. D. Rey, J. Chem. Phys. **126**, 094907 (2007); **127**, 104902 (2007).

[21] J. Yan and A. D. Rey, Phys. Rev. E **65**, 031713 (2002); Carbon **41**, 105 (2003).

[22] A. M. Sonnet and E. G. Virga, Phys. Rev. E **56**, 6834 (1997).

[23] M. E. Gurtin, *Thermomechanics of Evolving Phase Boundaries in the Plane* (Oxford University Press, New York, 1993).

[24] A. D. Rey, Phys. Rev. E **67**, 011706 (2003).

[25] A. Ludu, *Nonlinear Waves and Solitons on Contours and Closed Surfaces* (Springer-Verlag, Berlin, 2007).

[26] N. M. Ribe, Phys. Rev. E **68**, 036305 (2003).

[27] W. Kühnel and B. Hunt, *Differential Geometry: Curves - Surfaces - Manifolds* (American Mathematical Society, Providence, 2006).

[28] Y. A. Nastishin, K. Neupane, A. R. Baldwin, O. D. Lavrentovich, and S. Sprunt, arXiv:0807.2669.